Citation: Bricault, S., Dawson, M., Lee, J., Desai, M., Schwalm, M., Chung, K. S., DeTienne, E., Fagan, E., Li, N., Becker, A., et al (2024). Peripheral contributions to resting state brain dynamics. Nature Communications, 15(1), 10820. doi: 10.1038/s41467-024-55064-6

nature communications

Article

https://doi.org/10.1038/s41467-024-55064-6

Peripheral contributions to resting state brain dynamics

Received: 3 June 2022

Accepted: 28 November 2024

Sarah Bricault[1,2], Miranda Dawson[1,10], Jiyoung Lee[3,10], Mitul Desai[1], Miriam Schwalm[1], Kevin Sunho Chung[1], Elizabeth DeTienne[4], Erinn Fagan[1], Nan Li[1], Andrew Becker[1], Sureshkumar Muthupalani[5], Jan-Philipp Fränken[6], Dimitris A. Pinotsis[7,8] & Alan Jasanoff[1,8,9]

The correlational structure of brain activity dynamics in the absence of stimuli or behavior is often taken to reveal intrinsic properties of neural function. To test the limits of this assumption, we analyzed peripheral contributions to resting state activity measured by fMRI in unanesthetized, chemically immobilized male rats that emulate human neuroimaging conditions. We find that perturbation of somatosensory input channels modifies correlation strengths that relate somatosensory areas both to one another and to higher-order brain regions, despite the absence of ostensible stimuli or movements. Resting state effects are mediated by the same peripheral and thalamic structures that relay responses to overt sensory stimuli. The impact of basal peripheral input is reduced in a rat model of autism, which displays both lower somatosensory functional connectivity and insensitivity to vibrissa inactivation. These results demonstrate the influence of extrinsic influences on resting state brain phenotypes in health and disease.

It is widely believed that the mammalian brain performs intrinsic operations that are not directly actuated by environmental or bodily input. Brain activity in subjects "at rest"—in the absence of distinct tasks or stimuli—is typically interpreted as reflecting such operations[1,2]. Quintessential evidence for intrinsic brain processes comes from the observation of interregional temporal correlations in apparently spontaneous neural activity, a phenomenon termed resting state functional connectivity (rsFC)[3]. This phenomenon was first discovered using functional magnetic resonance imaging (fMRI) in awake humans[4] but has since been described in many species, under varying degrees of consciousness, and with reference to a diversity of recording methods. Although rsFC results have been shown to be contaminated by non-neural factors such as respiration and fidgeting[5,6], several studies have demonstrated a close correspondence between resting state neuroimaging data and underlying cellular physiology[7–11].

A fundamental question about resting state activity is whether it is genuinely governed by intrinsic aspects of brain function, as opposed to properties of the many peripheral inputs that impinge on the brain even in the absence of explicit stimuli or movements. Temporal variation of such inputs could arise from subtle environmental variations (*e.g.*, air currents, vibrations, temperature drifts) or internal physiological factors (*e.g.*, digestion, inflammation, hormonal processes) that escape the experimenter's ability to control or detect. Such unintended or "covert" peripheral influences on resting state brain activity are rarely considered in controlled experiments[12], but they could, in principle provide critical drive to neural dynamics during periods of

---

[1]Department of Biological Engineering, Massachusetts Institute of Technology, Cambridge, US. [2]Department of Biology, Massachusetts Institute of Technology, Cambridge, US. [3]Department of Neurobiology, Wellesley College, Wellesley, US. [4]Department of Electrical Engineering & Computer Science, Massachusetts Institute of Technology, Cambridge, US. [5]Division of Comparative Medicine, Massachusetts Institute of Technology, Cambridge, US. [6]Department of Psychology, University of Edinburgh, Edinburgh, United Kingdom. [7]Center for Mathematical Neuroscience and Psychology, Department of Psychology, City, University of London, London, United Kingdom. [8]Department of Brain & Cognitive Sciences, Massachusetts Institute of Technology, Cambridge, US. [9]Department of Nuclear Science & Engineering, Massachusetts Institute of Technology, Cambridge, US. [10]These authors contributed equally: Miranda Dawson, Jiyoung Lee. e-mail: jasanoff@mit.edu

apparent rest. If true, this would have important implications for the interpretation of rsFC results from subjects with putative disorders. For example, several psychiatric and neurodevelopmental diseases have been associated with extracerebral abnormalities that might be tractable candidates for treatment, should they be shown to account for symptoms detected by neuroimaging[13].

In this paper, we examine the hypothesis that resting-state brain activity arises in part from peripheral sensory sources and that extracranial factors could thus account for genotype-associated differences in resting-state data, for instance in disease models. We focus on the whisker-associated somatosensory system in rats because of the strong interhemispheric rsFC generally reported in vibrissa-associated regions of the rodent primary somatosensory cortex (S1)[14–17]. Using a combination of fMRI, central and peripheral inactivation, and computational modeling, we determine that ascending sensory input critically influences rsFC among both sensory and nonsensory brain regions, changing the interregional correlational structure of brain activity. Illustrating the biomedical importance of this phenomenon, we also show that differences in peripheral input strength from the face help explain a somatosensory hypoconnectivity phenotype observed in a widely studied rodent model of syndromic autism. Our work thus challenges purely brain-based interpretations of resting-state neuroimaging results and suggests that signatures of truly intrinsic brain function may be elusive.

Results

Immobilized, unanesthetized rats display strong resting state functional connectivity

Mechanistic studies of functional connectivity are usually performed using wide-field hemodynamic neuroimaging in rodents, but commonly utilized experimental conditions suffer from drawbacks[18]. Anesthetized preparations experience suppressed neural signaling that may not reliably model the majority of human resting-state studies[19,20]. In contrast, awake rodent preparations are prone to spontaneous movements that can affect neural dynamics[14,21] and potentially distort imaging data. To study resting state function in rodents without these confounds, we established conditions for fMRI in chemically immobilized, unanesthetized rats[22].

Animals were treated with the reversible muscle relaxant pancuronium and ventilated mechanically via an endotracheal tube. The stress hormone corticosterone was measured during habituation to these conditions over several days (Fig. 1a). Immobilization-induced stress levels were quantified as the ratio of corticosterone after versus before each acclimation session (Fig. 1b). These results showed that chemical immobilization with pancuronium was highly conducive to reducing stress during the acclimation period (*t* test $p = 0.015$, $n = 4$) and that acclimated, paralyzed animals were statistically indistinguishable from control animals that remained anesthetized instead of undergoing restraint (*t* test $p = 0.6$, $n = 4$ test and 7 control rats). Pancuronium-treated rats also showed a trend toward lower immobilization-induced stress than head-restrained animals (*t* test $p = 0.09$, $n = 4$ for both). Similar results were observed among absolute corticosterone concentrations measured after each immobilization or control treatment, albeit with greater inter-animal variability (Supplementary Fig. 1). These data indicate that the chemical immobilization approach could be applied humanely by the standards of the field[23–25]. In imaging experiments, the chemical immobilization technique also suppressed motion to levels similar to those observed under anesthesia while reducing motion much more effectively than head restraint (*t* test $p \le 0.025$ for all six degrees of motion, $n = 9$, 6; Fig. 1c and Supplementary Fig. 2).

Resting-state fMRI data were obtained from eleven chemically immobilized animals after habituation and used to compute estimates of functional connectivity between regions. In analyzing these data, we defined the amplitude of rsFC between each pair of regions of interest (ROIs) A and B using a general linear modeling (GLM) approach as the mean regression coefficient for voxels in region B against the average time course of signal changes in region A. Each rsFC amplitude thus reflects the amount of variance in B accounted for by signal changes in A.

A matrix of mean rsFC amplitudes quantified within brain regions (Supplementary Fig. 3) demonstrates widespread interregional relationships that are particularly prominent among somatosensory areas (Fig. 1d and Supplementary Fig. 4). We compared these measurements to analogous data from the same animals under 1.25–1.5% isoflurane anesthesia, and also to rsFC results from the separate set of awake head-restrained animals. The magnitudes of interhemispheric somatosensory connectivity were generally greater in chemically immobilized animals than in either anesthetized or head-restrained animals (Supplementary Fig. 5). Homotopic functional connectivity between left and right barrel cortex (S1BF), which processes vibrissa stimuli, was particularly notable in chemically immobilized animals (Fig. 1e) with respect to the other two preparations (Fig. 1f and Supplementary Fig. 6). Mean regression coefficients for homotopic S1BF rsFC were consistently higher in individual animals in the absence *vs.* presence of anesthesia (Fig. 1g), with differences significant with paired *t* test $p = 0.010$ ($n = 11$). Corresponding differences in resting state power are not observed (paired *t* test $p = 0.18$), indicating that differences in functional connectivity do not depend on the amplitudes of fMRI signal fluctuations (Fig. 1h, i). These data demonstrate that strong resting state functional connectivity signatures can be observed in the somatosensory system of awake rats in the absence of motion and anesthesia-related confounds.

Vibrissa inactivation diminishes somatosensory functional connectivity

We next directly tested the possibility that unintended, covert peripheral input might contribute to resting state phenomena in chemically immobilized rats. To do this, a separate set of animals was habituated to the imaging conditions and scanned both before and after bilateral inactivation of vibrissa-mediated sensation via a combination of whisker trimming and injection of bupivacaine into the posterior edge of the mystacial pads from which the vibrissae emerge (Fig. 2a). Comparison of pre- and post-treatment fMRI data demonstrates that vibrissa inactivation strongly alters resting state measures, suppressing functional connectivity metrics in somatosensory areas particularly including S1BF (Fig. 2b). Regression coefficient maps computed with respect to seed regions in S1BF correspondingly display sharp reduction in the extent of homotopic rsFC (Fig. 2c). These maps are similar when calculated with alternative statistical thresholding and display voxel-level responses to treatment that are statistically substantiated in a cluster of individual somatosensory voxels (Supplementary Fig. 7). When averaged over all of S1BF, mean regression amplitudes are 0.29 ± 0.04 before treatment and 0.17 ± 0.03 after treatment (Fig. 2d), a significant decrease of 41% (paired *t* test $p = 0.032$, $n = 8$). Control paired resting state datasets collected consecutively from untreated animals do not display significant effects ($p = 0.45$, $n = 7$; Supplementary Fig. 8). Differences between vibrissa inactivation and control datasets become even more apparent when the analysis is restricted to S1BF voxels showing substantial connectivity, as opposed to S1BF as a whole defined anatomically (Supplementary Fig. 9).

The effect of vibrissa inactivation is also apparent in an analysis where homotopic S1BF rsFC was analyzed dynamically in sliding 5-minute windows over time[26,27] (Supplementary Fig. 10). After treatment, regression coefficients were lower than the pre-treatment mean for about 80% of the time, indicating consistency of the reduction in rsFC metrics caused by vibrissa inactivation (*t* test $p = 0.008$, $n = 8$ animals). This analysis probes a spectral band between about 0.003 Hz and 0.1 Hz, limited by the window width and the hemodynamic response time course, respectively. Meanwhile, a comparison of fMRI spectral densities in the 0.01–0.1 Hz band (Fig. 2e and Supplementary Fig. 11) shows no significant difference upon inactivation treatment (*t* test $p = 0.34$), indicating that changes in the amplitude of activity fluctuations are not required for functional connectivity changes observed upon sensory deprivation.

Effects of vibrissa input deprivation extend to interactions between somatosensory areas and brain regions commonly associated with the brain's "default mode network" (DMN)[28,29]. Reductions in functional connectivity were observed between S1BF and ipsilateral cingulate, parietal, and retrosplenial cortex (Fig. 2f). Mean regression coefficients relating these three DMN-associated regions collectively to S1BF decreased from 0.26 ± 0.06 to 0.12 ± 0.02 upon vibrissa inactivation (Fig. 2g), a reduction by 40% that is significant with paired *t* test $p = 0.022$ ($n = 8$). Somatosensory deprivation treatment also reduces local ipsilateral functional connectivity within the S1 region itself. Regression coefficient maps associated with small S1BF seed regions show modest decreases throughout S1BF (Fig. 2h). When averaged bilaterally over S1BF (Fig. 2i), these decreases are significant with paired *t* test $p = 0.028$ ($n = 8$). These results together demonstrate that resting-state fMRI signal dynamics both within and beyond somatosensory brain regions depend on interactions with peripheral sense organs, even in the absence of explicit stimulation.

Electrophysiology confirms dissociation between neural activity and rsFC

Our resting state fMRI results suggest that changes in vibrissa-dependent changes in rsFC are not accompanied by analogous changes in mean S1BF activity, as indicated by spectral power. This suggests that vibrissa-dependent resting state input affects the synchrony but not the amplitude of spontaneous cortical activity. To confirm these fMRI power findings using a more direct measure of neuronal function, we recorded population-level electrophysiological signals before and after sensory manipulations equivalent to the fMRI experiments.

Three animals were implanted with unilateral transcranial electrodes above S1BF and habituated to chemical immobilization,

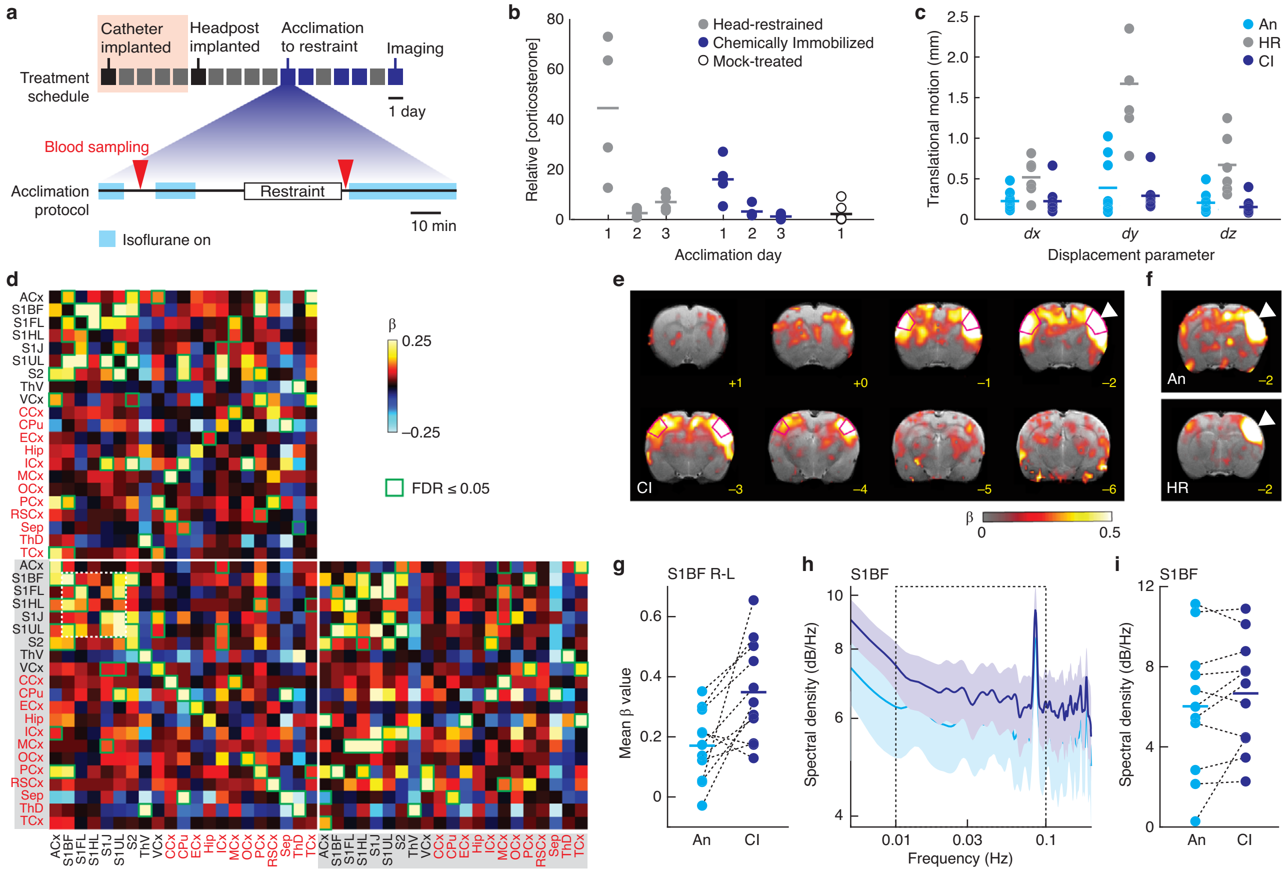

Fig. 1 | Resting-state functional connectivity in chemically immobilized rats. **a** Protocol for acclimation and imaging of chemically immobilized rats, showing the schedule of procedures over days (squares at the top) and the timing of individual acclimation sessions at the bottom. Catheter implantation (red shading, top) and blood draws (red arrowheads, bottom) were performed only on animals used for corticosterone monitoring. **b** Increase in relative corticosterone concentration (after/before treatment) induced by three successive sessions of acclimation to head restraint (gray, $n = 4$) or chemical immobilization (dark blue, $n = 4$) or during one session of mock treatment without immobilization stress ($n = 7$). **c** Motion parameters (maximal displacements *dx*, *dy*, and *dz*, all in mm) computed from fMRI data series measured using anesthetized rats (An, cyan), head-restrained animals (HR, gray), and chemically immobilized rats (CI, dark blue). **d** Functional connectivity matrix indicating mean regression coefficients (β) relating sensory and nonsensory brain areas (black and red labels, respectively). Seed regions are labeled on the vertical axis; shading = left hemisphere. Green boxes denote regions significantly nonzero across animals with FDR-corrected two-sided *t* test $p \leq 0.05$ ($n = 11$). The white dashed box highlights connectivity between left and right somatosensory regions. **e** Map of average of functional connectivity to a seed region in S1BF (arrowhead), in chemically immobilized animals. Regression coefficients indicated for voxels with two-sided *t* test $p \leq 0.01$ over $n = 11$ animals. Bregma coordinates in mm are indicated in yellow. **f** Regression maps indicating rsFC to S1BF seed regions (arrowheads) in anesthetized (top) and head-restrained (bottom) animals. Regression coefficients indicated for voxels with two-sided *t* test $p \leq 0.01$ over $n = 11$ (top) or 6 (bottom) animals. **g** Mean homotopic S1BF regression coefficients for anesthetized (cyan) *vs.* chemically immobilized (dark blue) animals, both $n = 11$ animals; difference significant with paired *t* test 0.010. **h** Power spectra of resting-state fMRI signal in S1BF under anesthesia (cyan) or chemical immobilization (dark blue). Shading denotes SEM over 11 animals. **i** Mean spectral densities in the 0.01–0.1 Hz band corresponding to the dashed box in panel (**h**) (difference not significant with paired *t* test $p = 0.18$).

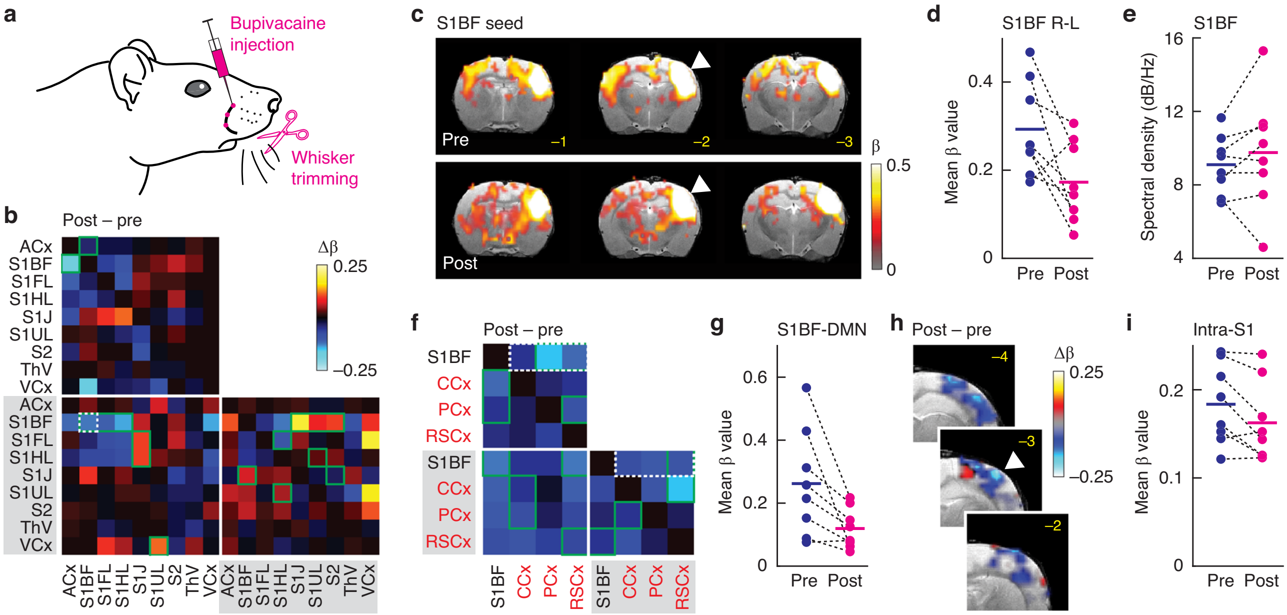

Fig. 2 | Vibrissa inactivation reduces functional connectivity measures. **a** Schematic of vibrissa inactivation procedure including bilateral whisker trimming and local anesthetic (bupivacaine) injection into the mystacial pads. **b** Change in functional connectivity strengths between sensory regions upon vibrissa inactivation. Color coding denotes the difference in regression coefficients after *vs.* before treatment. Green outlines denote significant differences with two-sided t test $p \le 0.05$ over animals ($n = 8$). The dashed box denotes left *vs.* right S1BF. **c** Seed-based maps over three coronal slices, showing functional connectivity to S1BF (arrowhead) before (top, Pre) *vs.* after (bottom, Post) vibrissa inactivation. Regression coefficients indicated for voxels with two-sided t test $p \le 0.01$ over $n = 8$ animals, and bregma coordinates (mm) noted in yellow. **d** Mean homotopic S1BF regression coefficients before (dark blue) *vs.* after (magenta) treatment in $n = 8$ animals (difference significant with paired t test $p = 0.032$). **e** Spectral density in the 0.01–0.1 Hz range before (dark blue) *vs.* after (magenta) vibrissa inactivation (difference not significant with t test $p = 0.34$). **f** Vibrissa inactivation-induced functional connectivity differences between S1BF and DMN-associated regions (red labels) in $n = 8$ animals. Color scale as in panel (**b**). **g** Mean connectivity strengths between S1BF and ipsilateral DMN-associated regions before (dark blue) *vs.* after (magenta) vibrissa inactivation. Values correspond to the average of dashed boxes in panel f, and the difference is significant with paired t test $p = 0.022$. **h** Map of average local functional connectivity to seed regions in S1BF (arrowhead), showing differences observed following vibrissa inactivation. **i** Quantification of ipsilateral functional connectivity to S1BF observed before (dark blue) *vs.* after (magenta) treatment in $n = 8$ animals.

followed by recording under conditions that paralleled the fMRI experiments. Measurements from individual animals in anesthetized and chemically immobilized conditions show expected slow-wave activity under deep anesthesia, but not under lighter sedation or chemical immobilization conditions, and little change in activity dynamics is observed following vibrissa inactivation (Fig. 3a). Consistent with reported isoflurane level-dependent trends[30], modest power decreases are observed between anesthetized and unanesthetized conditions, but little difference between pre-and post-vibrissa treatment spectra are seen (Fig. 3b). Comparison of spectral density across canonical frequency bands (Fig. 3c) shows corresponding results, with statistically significant decreases in low frequency delta (1–3 Hz) and alpha (8–12 Hz) band power upon cessation of anesthesia (paired t test $p = 0.014$ and $p = 0.029$, $n = 3$). There are no significant differences between recordings before *vs.* after vibrissa inactivation in the three low-frequency bands ($p \ge 0.12$), although a significant but small trend toward increased activity in the higher frequency beta band (12–35 Hz) is present in vibrissa-inactivated animals ($p = 0.043$).

Inhibition of thalamic sensory relay emulates peripheral blockade

If the effect of vibrissa inactivation on rsFC indeed reflects the removal of covert sensory input from the periphery, then we would expect alternative inhibitory interventions in the ascending somatosensory pathway to produce similar effects. To test this prediction, we examined the effect of thalamic inactivation on resting state activity in chemically immobilized animals. Eight rats were prepared with unilateral injection cannulae targeting the ventroposteriomedial thalamus (VPM), which acts as the principal relay for ascending input from the vibrissae to the cortex[31,32]. Resting-state fMRI data were obtained before and after infusion of 1.5 μL of 0.8 mM fluorescent muscimol (FM)[33], which produces long-lasting inactivation. Visualization of the drug by postmortem histology indicates that regions of approximately 1 mm from the site of infusion received substantial doses (Fig. 4a). Further assessment of FM spreading was possible in vivo on a volumetric basis in individual animals, by examining transverse relaxation time-weighted (T_2w) signal changes arising from fluid infusion into the tissue (Fig. 4b). Infusion leads to signal changes averaging up to about 15%, centered around VPM, confirming effective targeting by the inactivation procedure.

Functional connectivity metrics before and after FM treatment were computed using anatomically defined seed regions (Supplementary Fig. 2). Compared with untreated animals from Fig. 2, reduced homotopic S1BF connectivity is observed in the thalamic treatment subjects even before FM infusion, possibly due to disruptive effects of the implanted cannulae themselves on thalamic or surrounding tissue (Fig. 4c). Homotopic rsFC in S1BF was further reduced following thalamic inactivation, however, emulating the effects of vibrissa inactivation in the data of Fig. 2c. This effect was unlikely to arise from damage, given the low flow rates used for FM infusion and the fact that cannulae were chronically placed long before the experiments. ROI-averaged results indicate that the FM treatment leads to a 69% reduction of homotopic S1BF connectivity strength, which is significant with paired t test $p = 0.036$ ($n = 8$) (Fig. 4d). When this analysis is restricted to S1BF voxels showing the highest rsFC amplitudes, the effect of thalamic inactivation is more significant (t test $p = 0.019$) (Supplementary Fig. 9). Importantly, when the change in S1BF rsFC is compared quantitatively with the T_2w signal change produced by spreading of FM into the ventral thalamus (Fig. 4e), a significant correlation coefficient of $R = -0.78$ is observed ($p = 0.023$, $n = 8$ animals).

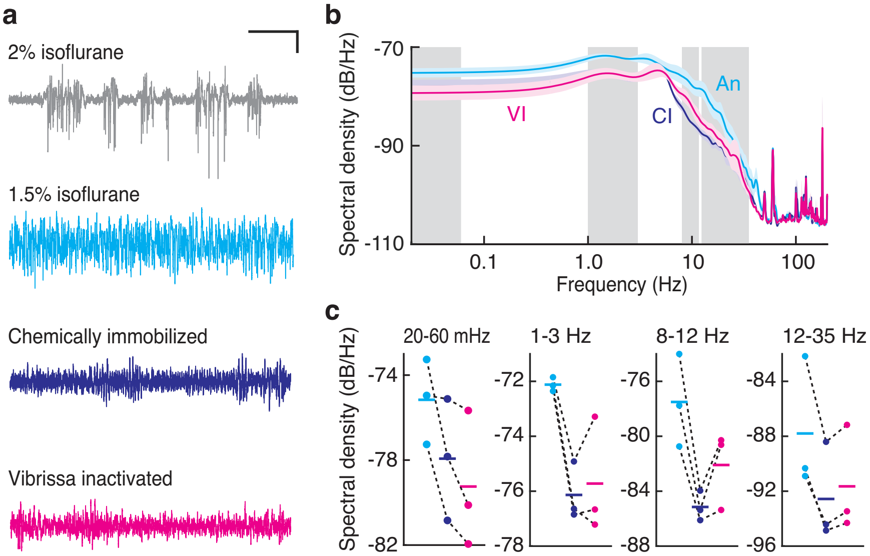

Fig. 3 | Electrocortigraphy in S1BF under treatment conditions. a Representative recordings of electrical activity in S1BF during deep and moderate anesthesia and in the unanesthetized but chemically immobilized state before (dark blue) and after (magenta) vibrissa inactivation. Vertical scale bar = 0.2 mV, horizontal scale bar = 5 s. **b** Power spectra of electrical signals under conditions color-coded in panel (**a**). Colored shading denotes SEM over $n = 3$ animals. **c** Spectral density in select bandwidths comparing power density under 1.5% isoflurane anesthesia and before *vs.* after vibrissa inactivation, for the four bands denoted by gray boxes in panel (**b**).

Similar findings are obtained when S1BF rsFC is compared with T_2w signal change in posteromedial thalamus, which also conveys vibrissa-related input to somatosensory cortex[34] (Supplementary Fig. 12). These results are consistent with the explanation that sensory input relayed by the thalamus contributes to rsFC in the somatosensory system.

Tonic somatosensory input simulates the consequences of inactivations on rsFC

To explain the effects of vibrissa and thalamic inactivation on rsFC, we surmised that basal sensory influences in the scanner, possibly including subtle air currents, blood flow in the vibrissa pad, and respiratory movements, provide an unintended drive to somatosensory pathways during resting state fMRI acquisition; coherent bilateral sensory responses to this drive could account in part for homotopic S1BF functional connectivity. If this hypothesis were true, then the purposeful addition of a tonic stimulus would be expected to alter rsFC in the somatosensory cortex in a manner similar to that achieved by sensory pathway inactivation. To test this idea, we designed an MRI-compatible stimulator that permits transient or continuous delivery of pulsed pressurized air flows to each side of the rat face during scanning. We established efficacy of the system by performing conventional block-design fMRI using transient unilateral air pulse trains (30 s at 10 Hz) in CI rats to stimulate each side of the face (Fig. 5a). We found that each unilateral stimulus was effective in eliciting reproducible sensory responses in contralateral S1 (Fig. 5b), with mean signal change amplitudes of 0.33 ± 0.04% that were similar on both sides (Fig. 5c). Examination of corresponding fMRI signal change maps (Fig. 5d) indicates that each stimulus-evoked weak ipsilateral responses in additional to more pronounced contralateral fMRI signal changes.

We acquired resting state fMRI from the same set of animals in the presence or absence of continuous 10 Hz pulsed airflow. Functional connectivity was assessed between regions shown to be activated by airflow in the block stimulation experiments. ROIs were defined as the collection of voxels falling within the cortex for which the p-value for sensory responses across animals was 0.05 or less. Seed-based maps from this analysis revealed both interhemispheric S1 and intrahemispheric S1-thalamus functional connectivity (Supplementary Fig. 13). Interhemispheric S1 measurements underwent a substantial decrease in the presence of the airflow (Fig. 5e). The mean rsFC strength was reduced by 31%, from 0.29 ± 0.11 without airflow to 0.20 ± 0.11 with airflow (Fig. 5f), a significant difference with paired t test $p = 0.04$ ($n = 7$). These results thus parallel the vibrissa and thalamus inactivation experiments in demonstrating the importance of peripheral sensory factors for resting state brain phenotypes; the results also indicate that a stimulus that elicits phasic somatosensory responses can alter rsFC in corresponding regions when delivered in tonic form.

Sensory deprivation alters estimated effective connectivity in the resting state

The experiments of Figs. 2–5 show that somatosensory rsFC is sensitive to altered input from outside the brain, but the neural changes underlying these observations are uncertain. We wondered in particular whether changes in basal input affect the somatosensory system simply by changing the drive amplitude to an otherwise stationary brain network, or whether effective connectivity within the network itself adapts to changes in the input, via adjustments to the coupling constants that determine the characteristics of information flow between brain regions (Fig. 6a)[35]. To distinguish these alternatives, we fit the resting state fMRI data from S1BF and ventral thalamic ROIs to dynamic causal models (DCMs) and assessed the probability that competing model formulations account for the results of our inactivation experiments[36,37]. We compared four models[38] (Fig. 6b) in which (1) neither effective connectivity nor input drive changes as a result of the treatment; (2) only effective connectivity changes; (3) only input drive amplitude changes; or (4) both connectivity and input drive change. These models were applied separately to data from vibrissa and thalamic inactivation experiments ($n = 8$ and 9, respectively) and results were expressed as the exceedance probability (EP) of each model, defined as the probability that a given model better accounts for the data than all other models[39].

For the vibrissa inactivation data (Fig. 6c), model 2 was the most likely model (EP = 0.59), with model 4 as a reasonably close second (EP = 0.34), while models 1 and 3 had negligible contributions (EP ≤ 0.06). This indicates that changes in interregional effective connectivity with or without changes in region-specific input amplitudes are sufficient to account for the effects of vibrissa treatment on fMRI time courses in S1BF and the sensory thalamus. For the unilateral

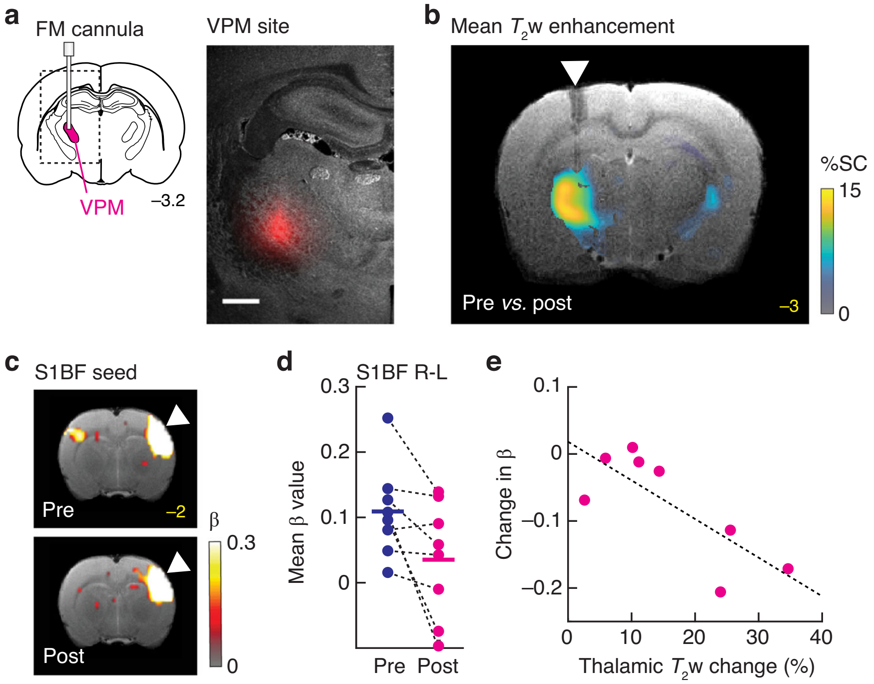

Fig. 4 | Thalamic inactivation reduces bilateral S1BF functional connectivity. **a** Targeted inhibition of thalamic neural activity is achieved by injecting fluorescent muscimol (FM) via a cannula implanted into VPM (magenta). The image at right corresponds to the dashed rectangular area in the schematic at left and shows FM distribution (red) in a representative animal. Scale bar = 1 mm. **b** Average T_2w signal increase observed following FM infusion. **c** Average map of functional connectivity to an S1BF seed region before (top) and after (bottom) FM infusion. Regression coefficients indicated for voxels with two-sided *t* test $p \leq 0.01$ over $n = 8$ animals. **d** Mean homotopic S1BF regression coefficients before (dark blue) *vs.* after (magenta) FM infusion in $n = 8$ animals, showing a significant decrease with paired *t* test $p = 0.019$. **e** Correspondence between FM spread indicated by T_2w signal change in ventroposterior thalamus and change in homotopic rsFC regression coefficient. The dashed line indicates linear regression fit with correlation coefficient $R = -0.78$ ($p = 0.023$, $n = 8$ animals).

thalamic inactivation experiment of Fig. 4, we found that model 2 was unambiguously best in accounting for the data, with an EP of 0.97 (Fig. 6d). This indicates that changes in effective connectivity but not region-specific input amplitudes were most probably induced by FM injection into VPM.

Because the results of vibrissa and thalamic inactivation were both best explained as changes in effective connectivity, we examined the estimated changes in interregional coupling strengths in greater detail. Applying a statistical technique known as parametric empirical Bayes inference (PEB)[40,41], we compared nested variants of model 2 that include changes in unidirectional and bidirectional interactions among the S1BF and thalamic nodes diagrammed in Fig. 6b (Supplementary Fig. 14). When analyzed this way, high probability parameter changes ($p \geq 0.99$) are predicted from each perturbation experiment: bilateral vibrissa inactivation is associated with approximately symmetric decreases by 0.06–0.08 Hz in effective connectivity coupling constants between left and right S1BF regions, while unilateral thalamic inactivation results in an asymmetric decrease by 0.08 Hz in activity propagation from S1BF on the treatment side to its contralateral mirror image.

Autism model rats display reduced influence of somatosensory input on rsFC

We next asked whether brain-periphery interactions could contribute to resting state phenotypes associated with brain disorders. Autism spectrum disorders (ASDs) have been related to atypical rsFC findings, and these are usually ascribed to characteristics of intrinsic brain function[42]. Animal models of autism have also been shown to exhibit alterations in peripheral sensory function[43], however, raising the question as to whether ASD-associated rsFC characteristics might also be influenced by factors outside the brain. We examined this issue in a rat model of fragile X syndrome (FXS)[44], a widely studied ASD. Although FXS animals display no obvious abnormalities in mystacial pad morphology (Supplementary Fig. 15), they have been reported to exhibit hypersensitivity to somatosensory stimuli in behavioral tests[45] and reduced interhemispheric rsFC in previous fMRI studies[46]. Although the rsFC phenotype of FXS rats may partly reflect differences in vascular reactivity (Supplementary Fig. 16), we considered it plausible that FXS animals might display aberrant peripheral somatosensory contributions to resting state dynamics as well.

Five FXS model rats containing deletions of the fragile X mental retardation gene *FMR1* were habituated to chemical immobilization and investigated using resting state fMRI before and after vibrissa inactivation analogous to the experiments of Figs. 2, 7a). Comparison of resting state fMRI data from FXS versus wild-type (WT) animals before treatment reveals substantial differences in sensory functional connectivity (Fig. 7b). Somatosensory connectivity, in particular, is different, as revealed by S1BF rsFC maps (Fig. 7c). Mean regression coefficients for homotopic S1BF functional connectivity are 0.29 ± 0.04 for WT rats ($n = 8$) versus 0.10 ± 0.03 in FXS animals ($n = 5$), a significant difference of 66% (unpaired *t* test $p = 0.0054$). We reasoned that if the reduced rsFC in FXS rats is due in part to attenuated contributions of peripheral input in the resting state, then vibrissa inactivation treatment should produce a little further reduction in rsFC in these animals. In fact, both seed-based maps (Fig. 7c) and quantification of homotopic regression coefficients in FXS animals (Fig. 7d and Supplementary Fig. 9) indicate that vibrissa inactivation produces negligible effects. Amplitudes of homotopic S1BF rsFC coefficients R-L are 0.10 ± 0.04 before and 0.05 ± 0.05 after vibrissa inactivation, a statistically insignificant difference ($p = 0.28$, $n = 5$).

Differences in the coupling of S1BF to nonsensory DMN-associated areas are also observed between FXS and WT animals. Regression coefficients relating S1BF to cingulate, parietal, and retrosplenial cortical regions were reduced on average in FXS rats,

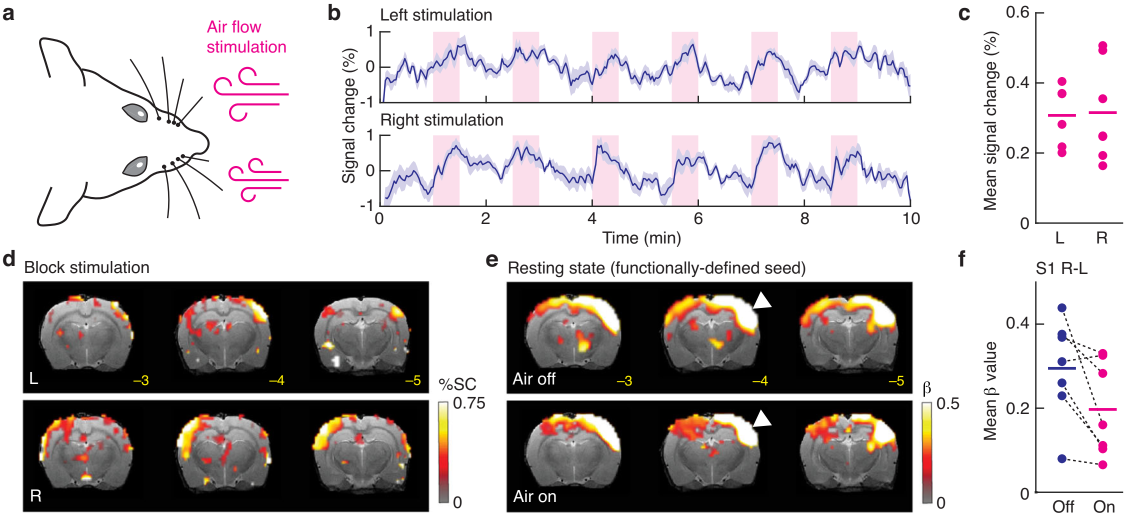

Fig. 5 | Somatosensory input alters rsFC in regions responsive to phasic stimulation. a Somatosensory input is delivered using pulsed air flows delivered to each side of the face. **b** Signal changes over time in S1, in response to phasic airflow stimulation delivered in blocks (pink rectangles) to the left (top) and right (bottom) sides of the face. Shading around time courses denotes SEM over $n = 6$–7 animals. **c** Mean responses to block stimulation on the left and right sides over $n = 6$–7 animals. **d** Maps of the mean response to left and right block stimulation in (**b**). Results for voxels with significant responses over animals were shown (two-sided t test $p \leq 0.05$, $n = 7$). Bregma coordinates in mm are indicated in yellow. **e** Seed-based maps of rsFC acquired in the absence (top) and presence (bottom) of tonic bilateral air flow stimulation. Seed locations in S1 (arrowheads) correspond to functional responses in (**d**). Regression coefficients indicated for voxels with t test $p \leq 0.01$ over $n = 7$ animals. **f** Mean homotopic S1BF regression coefficients in the absence (dark blue) *vs.* presence (magenta) of tonic airflow stimulation over $n = 7$ animals, showing a significant difference with paired t test $p = 0.04$.

compared with WT (t test $p = 0.013$) (Fig. 7e). As with homotopic somatosensory functional connectivity, vibrissa inactivation had no obvious effect (t test $p = 0.48$) on the mean rsFC amplitude relating S1BF to the DMN regions (Fig. 7f). These results indicate that the FXS model exhibits a resting state phenotype that parallels the effects of vibrissa-mediated sensory deprivation in WT animals, suggesting that rsFC phenomena in FXS rats can be explained partly in terms of altered peripheral contributions to resting-state brain activity.

Discussion

We have shown that the inactivation of a peripheral somatosensory organ—the vibrissae of the rat—and its thalamic relay structure exert substantial effects on fMRI-based resting state functional connectivity results. Physiological perturbations we applied show that these effects involve the same pathways that mediate normal sensation, but they are observed in the absence of explicit time-varying stimuli, under conditions where no sensory neural responses are normally expected. In this respect, our results differ notably from previous findings that functional connectivity is altered by the presence of ongoing overt sensory input such as background visual stimuli[47–49], which drive more predictable responses in the brain. Consequences of the peripheral sensory manipulations we performed impinge on brain networks both in the somatosensory cortex and beyond, as highlighted by effects of sensory deprivation on coupling between somatosensory cortex and DMN-associated brain structures, adjustment of interregional effective connectivity strengths following the manipulations, and adaptation of somatosensory activity to similar levels even after inhibition of input.

The relevance of these results to human resting-state fMRI studies is emphasized by the fact that our experiments were conducted in an unanesthetized, movement-free animal preparation that emulates human fMRI subjects by avoiding confounds present in alternative animal models. The importance of our findings for analysis of neurological disorders is illustrated by the absence of somatosensory deprivation effects on rsFC in a syndromic autism model, FXS rats, suggesting that the difference between normal and atypical subjects may arise in part from perturbations in structures outside the brain. Our results thus argue for a broad view of resting state analysis that acknowledges the importance of bodily and environmental factors as partial drivers of healthy or abnormal brain dynamics. Our findings importantly extend the evidence for extracerebral involvement in resting-state brain phenotypes. Recent attention has focused in particular on the effects of spontaneous movements[6], which relate systematically to sensorimotor brain function and can also corrupt neuroimaging data in ways that can be misinterpreted as neural activity correlations. Animals undergoing such movements are not "resting" to the same extent as the rats we studied here, which were chemically immobilized using a skeletal muscle blocker. Although it is still possible that passive motion from ventilation or autonomic smooth muscle activity contributes in some way to the rsFC phenomena we observed, centrally actuated movements such as whisking or blinking could not occur. Somatosensory inputs probed in our experiments are thus more unambiguously peripheral in origin, as well as independent of volitional behavior and respiration. Our results consequently demonstrate that feed-forward signaling from the body to the brain is a notable contributor to what are usually viewed as brain-driven resting state results.

Other peripheral factors previously identified as influences in resting state fMRI, primarily in humans, include neuropathies[50,51], congenital sensory defects[52,53], inflammation[54–57], and gut microbiota[58,59]. Key differences distinguish our findings from results implicating these factors, however: First, these other phenomena involve long-term physiological processes likely to be accompanied by plasticity both peripherally and centrally. In contrast, the inactivation manipulations we performed are acute, so our results reflect more or less instantaneous perturbation of signaling, as opposed to the reorganization of any of the pathways or structures involved. Second, pathological influences like inflammation often cause discomfort and thus introduce new stimuli; this is again in contrast to our inhibitory treatments, which were designed to remove basal signal sources present in the resting state—vibrissa and thalamic inactivation we performed both involve the injection of drugs expected to block most neural signaling emanating from the injected structures without activating new inputs. Third, because we examined inactivation effects at an individual animal level, our results are not subject to the influence of

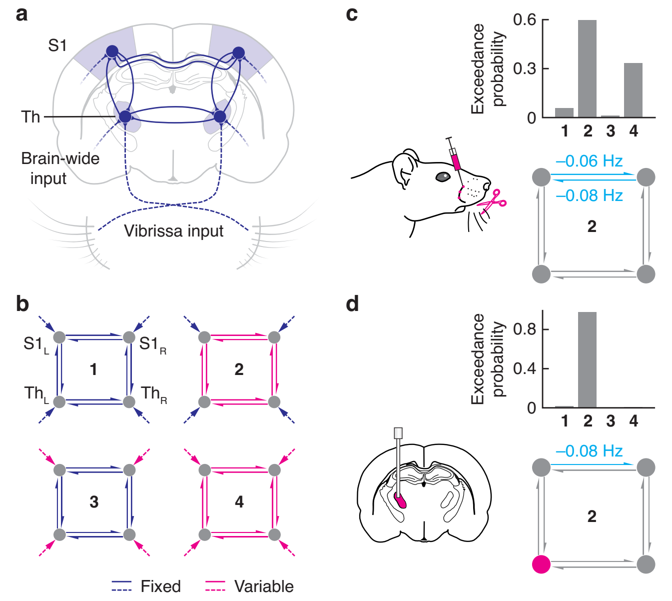

Fig. 6 | Effective connectivity changes induced by inactivation treatments. **a** Schematic showing brain regions included as nodes in DCM analysis, with input to each region from brain-wide or peripheral sources included or excluded in competing model formulations. **b** Four model formulations that account for fixed (blue) or treatment-dependent (magenta) connectivity among brain region nodes (solid arrows), as well as fixed or treatment-dependent input to each region (dashed arrows). Inputs, where present, are taken to combine central and peripheral sources. **c** Exceedance probabilities (top) indicate that both model 2 and model 4 potentially explain the results of the vibrissa inactivation experiment (schematic). When model 2 is fit to the data (bottom), DCM analysis estimates reductions in homotopic S1 effective connectivity strengths (cyan), but not connectivity involving thalamic regions. **d** Exceedance probabilities (top) indicate that model 2 best accounts for the results of the thalamic inactivation experiment (schematic). Parameter estimates using model 2 (bottom) indicate asymmetric reduction (cyan) in effective connectivity from S1 on the treatment side (magenta node) to the untreated side.

comorbidities or sampling biases that might complicate human studies in which results from separate test and control cohorts are compared.

Understanding the basis of resting-state brain activity is important because of its presumed relationship to spontaneous cognition and behavior[1,2]. On a more applied level, resting state phenomena are also important as candidate biomarkers for a variety of neurological and neurodevelopmental conditions[60,61]. For this reason, we studied the relevance of our somatosensory rsFC findings to a rat model of FXS, a syndromic form of autism[62]. We found that unanesthetized FXS rats display sharply reduced somatosensory functional connectivity under unperturbed conditions, harmonizing with prior observations of generalized cortical hypoconnectivity in human FXS patients[63] and in an anesthetized FXS mouse model[46]. Our result suggests that covert sensory input plays a subsidiary role in the mutants compared to wild-type rats. This idea is corroborated by the finding that vibrissa inactivation in FXS rats produces no discernable change in homotopic S1BF functional connectivity, although this result may be influenced by the already low pre-treatment rsFC and apparently lower vascular reactivity observed in the mutant animals.

The finding that somatosensory resting state hallmarks are perturbed in the FXS model is consistent with previous reports of somatosensory phenotypes in ASDs[45,64,65]. Hypersensitivity to mechanical stimuli has been described in both human subjects and autism models. Recent studies have shown that peripheral tactile receptors are aberrant in *Mecp2* and *Shank3* ASD mouse mutants and that a peripherally acting GABA agonist attenuates somatosensory hypersensitivity in a number of autism models including FXS mice[43]. If peripheral components of somatosensation are chronically hyperactive in ASD models, one might have expected vibrissa inactivation to have a greater impact on mutants than on wild-type animals, but the opposite is observed. Potential explanations for this include the possibility that the characteristics of basal peripheral input are less conducive to bilateral rsFC in FXS animals, or the possibility that compensatory changes in brain circuitry limit the influence of covert peripheral input in the mutant rats. Either way, the fact that FXS rats and wild-type animals differ clearly with regard to the role of somatosensory input in resting state fMRI attests to the importance of interactions between brain and periphery in co-determining resting state phenotypes associated with neurological disorders.

Our study suggests a number of overall conclusions and future directions. First, the finding of distinct sensory contributions to resting state activity—even in the absence of motion or stimulation—suggests a need to govern environmental variables that could interact with sensory pathways in all resting-state fMRI studies while highlighting the difficulty of establishing consistent “resting” conditions that apply across subjects and measurement contexts. This is especially true in cases where environmental factors might interact differently with behaviorally or genetically defined cohorts, as in the FXS *vs.* wild-type rat comparison we performed. Second, it is natural to ask which other sensory processes, including interoceptive functions[66] or stimulus-independent visual activity[67], might also influence resting state brain dynamics in unexpected ways. The involvement of other pathways could be investigated in further studies, similar to ours, that use perturbation methods in conjunction with neuroimaging in unanesthetized animals that model the physiology of human subjects. Third, it is of outstanding interest to further understand the biological mechanisms of coupling between peripheral and central physiology in the resting state. More can be learned, for instance, about which cellular components relay resting state sensory inputs, what temporal properties they exhibit, and how bodily and environmental factors could act on peripheral inputs to influence correlated brain activity. Studying these properties could provide substantial insights into organism-wide origins of cognition and behavior.

Methods

Animal subjects

All animal procedures were performed in strict compliance with US Federal guidelines, with oversight by the MIT Committee on Animal Care under approved protocol number 0721-059-24. Male Sprague-Dawley rats (250–350 g) were purchased from Charles River Laboratories (Wilmington, MA). Male fragile X syndrome (FXS) model rats (250–350 g) lacking a functional *FMR1* gene were obtained from Envigo. All animals were housed and maintained on a 12 h light/dark cycle with *ad libitum* access to food and water.

Drugs and reagents

Drugs and reagents were purchased from Sigma-Aldrich (St. Louis, MO) unless otherwise noted.

Surgical procedures

In preparation for imaging, rats were implanted with custom-made PEEK headposts so that their heads could be fixed in place during imaging. Animals were anaesthetized with 3% isoflurane, shaved, and mounted in a rodent stereotaxic device (David Kopf Instruments, Tujunga, CA). Heart rates and blood oxygenation levels were monitored by a pulse oximeter (Nonin Medical, Plymouth, MN), and the isoflurane was maintained at 2%. The scalp was retracted, and the headpost was placed approximately over the bregma. In animals undergoing acclimation to physical restraint, four beryllium copper screws were inserted such that they penetrated the skull but not the

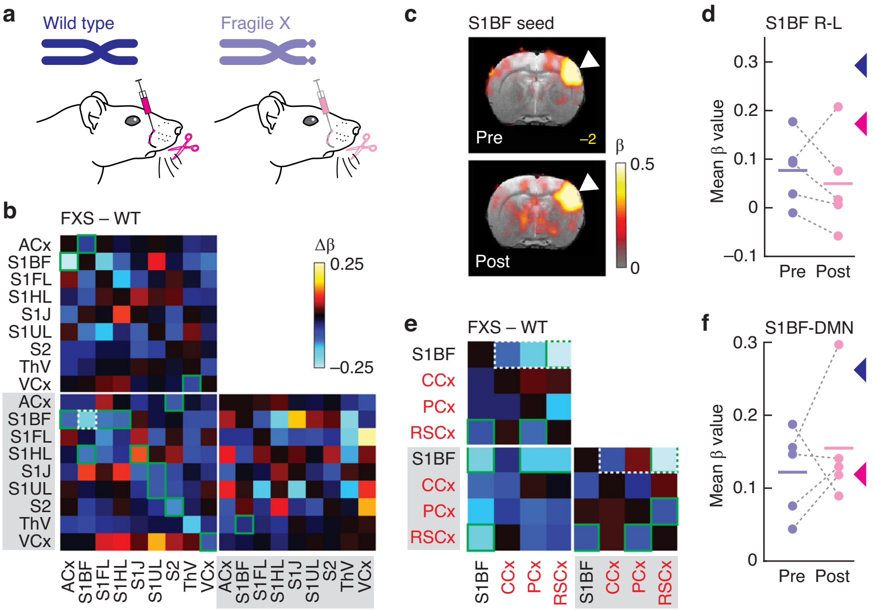

Fig. 7 | Vibrissa treatment produces minimal effects in a syndromic ASD model. **a** The vibrissa treatment procedure of Fig. 2 was applied to wild-type (WT) and fragile X syndrome (FXS) model rats. **b** Genotype-dependent differences in interregional regression coefficients indicate hypoconnectivity in FXS animals between left and right S1BF (dashed box) as well as other somatosensory regions. **c** Maps of rsFC regression coefficients to S1BF seed regions before (top) and after (bottom) vibrissa inactivation in $n = 5$ FXS model animals. **d** Quantification of mean homotopic S1BF regression coefficients before (light blue) and after (light magenta) vibrissa treatment in five FXS animals (difference not significant with paired t test $p = 0.28$), compared with results from WT animals indicated by arrowheads at right (blue before, magenta after treatment). **e** Reduction in connectivity strengths between S1BF and brain regions associated with the DMN in FXS animals, with respect to WT. **f** Quantification of S1BF-DMN connectivity strengths before and after vibrissa treatment in $n = 5$ FXS animals (difference not significant with t test $p = 0.48$), again with respect to WT values indicated by color-coded arrowheads.

dura to provide additional support to the headpost. The headpost and screws, where used, were secured using C&B Metabond dental cement (Parkell, Edgewood, NY). Each rat was given a subcutaneous injection of buprenorphine (MIT pharmacy) at a dose of 0.05 mg/kg for analgesia at the end of surgery, and once a day for two days following surgery. Rats were allowed to recover from surgery for at least three days before acclimation began.

Acclimation to chemical immobilization

All animals that were imaged under chemical immobilization underwent an acclimation procedure. The acclimation period lasted approximately one week, consisting of two consecutive days, one break day, and two final consecutive days. On the final day of acclimation, MRI scan noises were played to the animal to simulate the auditory environment of the scanner. For a subset of animals, corticosterone measurements were taken at the beginning and end of the procedure each day. For these animals, the acclimation was performed at the same time of day ± 30 min throughout the acclimation week.

Each individual day of acclimation began with the animal being weighed and then anesthetized with 3% isoflurane. Either a tail vein catheter was established or, for animals with a chronically implanted jugular vein catheter, the catheter was briefly flushed with heparinized saline. If corticosterone measurements were being taken, the animal was quickly placed in a tube restraint that allowed for access to the chronically implanted jugular vein catheter. These animals were allowed to recover from the isoflurane anesthesia and as soon as they displayed active motor behavior or a substantial motor response to a tail pinch, a control (pre-experiment) blood sample was drawn. The animals were then re-anesthetized with 3% isoflurane and removed from the tube restraint.

Animals were then intubated ventilated, and placed on a heating pad to maintain their body temperature. Heart rate, expired CO_2, breathing rate, and SpO_2 (peripheral capillary oxygen saturation) were monitored and recorded starting at this point, and isoflurane was reduced to 1%. Midazolam (1.25 mg/kg) and a bolus dose of pancuronium at 1.25 mg/kg were administered via the catheter. Pancuronium was delivered continuously at 1.5 mg/kg/h for the remainder of the acclimation. Five minutes after the bolus dose of pancuronium, the isoflurane flow was stopped and animals were allowed to recover for 15 min. During this period, animals were monitored closely, and in the case of incomplete paralysis (due to catheter failure), the acclimation was immediately terminated, the pancuronium reversal agent neostigmine was administered, and the animal was allowed to recover.

After the 15 min recovery from isoflurane, the experimentally defined 30 min acclimation period began. Animals were covered with an opaque box to simulate the darkness of the scanner environment, and if it was the final day of acclimation, recorded scanner noises were played. Mock-treated animals were maintained on isoflurane for 30 min instead of acclimation. At the end of the treatment period, blood was drawn in animals for which corticosterone was being measured. The pancuronium reversal agent neostigmine (0.25 mg/kg) was administered at this time, sometimes in conjunction with atropine (0.135 mg/kg), which we found aided the recovery of the respiratory system. Isoflurane was reintroduced at 1% to prevent the animals from extubating themselves prior to regaining the ability to regulate their breathing.

Animals recovered from the paralysis at different rates, and the full recovery could take as little as 20 min or as long as 90 min. For animals whose recovery took longer than ~ 45 min, a second dose of neostigmine (0.25 mg/kg) and sometimes atropine (0.135 mg/kg) were administered. Once animals demonstrated the ability to regulate respiration, they were taken off the ventilator, and the isoflurane was turned off. Oxygen was delivered until the animals began to move, at which point they were gently extubated and returned to their home cage. Animals were monitored for at least an hour after the procedure to ensure successful recovery.

Acclimation to head restraint

All animals that underwent imaging or corticosterone measurement under head restraint were acclimated to the restraint procedure over 3–4 days. The procedure was comparable to that described for chemical immobilization above, with the exception that no paralytic was given and animals were more securely wrapped and head-fixed to prevent movement and to reduce the possibility of injury.

Corticosterone measurements

A total of four test animals and seven control animals were examined to test the effects of restraint techniques on stress hormone production. Corticosterone levels were measured to assess stress levels in the animal preparations. To permit corticosterone quantification, we collected blood at two-time points, as described above. Immediately after the ~ 0.5 mL of blood was drawn, it was placed into treated tubes to prevent clotting and refrigerated. Once all blood samples had been collected, an ELISA kit was used to measure the concentration of corticosterone for each animal at each time point. Relative corticosterone concentrations reported were calculated by computing the ratio of ELISA results after *vs*. before each restraint session. This normalization procedure corrected for inter-animal and inter-trial variability in the performance of the assay, as reflected in absolute ELISA measurements.

Preparation of animals for functional imaging

Immediately prior to imaging experiments, rats were anesthetized using 3% isoflurane and maintained at 2% isoflurane during preparation. Animals were intubated and ventilated (60 strokes/min, 9.5 mL stroke volume, 2 m tubing from ventilator to rat), and a tail vein catheter was established for drug delivery in cases where a jugular vein catheter was not already present. Animals were then placed onto an imaging cradle and secured in place via screws attached to the implanted headpost. Isoflurane was reduced to 0.75%, and 1 mg/kg pancuronium was administered, followed by continuous delivery of 1.5 mg/kg/h pancuronium thereafter. Respiration, heart rate, and blood oxygen saturation were monitored, and temperature was maintained with a circulating warm water pad (Gaymar, Orchard Park, NY) for the remainder of the procedure. In some cases, imaging was performed under anesthesia. In preparation for imaging without anesthesia, isoflurane was stopped and the animal was given at least 15 min to recover.

MRI data acquisition

To compare characteristics of resting state fMRI data from different animal preparations, six animals were used for head-restrained scans, and 11 animals were used for anesthetized and chemically immobilized scans. Three additional animals were excluded from the chemical immobilization and anesthesia datasets on the basis of a poor SNR ratio; anesthetized and unanesthetized scans from these animals were equally affected. Chemically immobilized animal cohorts used to assess specific perturbations are described in subsequent sections.

For fMRI of chemically immobilized rats throughout this study, imaging was performed using a 7 T Biospec MRI scanner (Bruker, Ettlingen, Germany) scanner operating with a cross coil volume transmit, surface receive configuration (Doty Scientific, Columbia, SC). A rapid acquisition with refocused echoes (RARE) pulse sequence was used to acquire transverse relaxation time-weighted (T_2w) anatomical images, with the number of averages (NA) = 16, matrix size = 256 × 256, FOV = 2.2 cm × 2.2 cm, slice thickness = 1 mm, TR = 2500 ms, effective TE = 44 ms, and RARE factor = 8. Functional imaging was generally performed using an echo planar imaging (EPI) pulse sequence applied with matrix size = 53 × 53, FOV = 2.2 cm × 2.2 cm, slice thickness = 1 mm, TR = 2500 ms, and TE = 13 ms. For the whisker pad inactivation experiments in wild type and FXS rats, EPI image series were acquired with matrix size = 64 × 64, FOV = 2.56 cm × 2.56 cm, slice thickness = 1 mm, TR = 2000 ms, and TE = 16 ms.

For analysis of head-restrained animals, imaging was performed using a 9.4 T Biospec MRI scanner (Bruker) scanner operating with a volume coil transmit and receive configuration. A rapid acquisition with refocused echoes (RARE) pulse sequence was used to acquire T_2w anatomical images, with the number of averages (NA) = 4, matrix size = 256 × 256, FOV = 2.5 cm × 2.5 cm, slice thickness = 1 mm, TR = 2541 ms, effective TE = 56 ms, and RARE factor = 8. For functional imaging, EPI image series were acquired with matrix size = 100 × 100, FOV = 2.5 cm × 2.5 cm, slice thickness = 1 mm, TR = 2000 ms, and TE = 30 ms.

Vibrissa pad inactivation

Eight chemically immobilized WT animals and five FXS animals were used for analyses of the effects of vibrissa pad inactivation on resting state fMRI data acquired as described above. An additional WT animal was imaged but excluded because of low SNR, and no FXS animals were excluded. To remove all sensations coming from the whisker pad in these experiments, all whiskers were trimmed down to the skin level bilaterally. Furthermore, three 15 μL injections of 0.5% bupivacaine were made along the posterior edge of each whisker pad bilaterally, as diagramed in Fig. 2a to ensure there was no residual sensation. MRI scan series were performed before and after vibrissa pad inactivation and animals were temporarily withdrawn from the scanner to permit vibrissa treatments.

Thalamic inactivation

Eight chemically immobilized animals were included in a dataset involving thalamic inactivation via muscimol infusion during fMRI; an additional animal was excluded due to poor cannula placement. Prior to experimentation, rats were implanted with infusion cannulae targeting VPM, using surgical procedures similar to those described above. Animals were anaesthetized with 3% isoflurane and maintained at 2% isoflurane, shaved, and mounted in a rodent stereotaxic device (Kopf). Each rat was given a subcutaneous injection of buprenorphine (MIT pharmacy) at a dose of 0.05 mg/kg for analgesia at the end of surgery, and once a day for two days following surgery. The scalp was retracted and 28 G holes were drilled into the skull 3.2 mm posterior and 3 mm lateral to bregma, unilaterally. 28 G cannula guides (Plastics One, Roanoke, VA) designed to project 2 mm below the surface of the skull were implanted and secured using C&B Metabond dental cement. Small plastic head posts were implanted to facilitate head fixation during the MRI experiments. Finally, 32 G dummy cannulae designed to fit the guide cannulae were inserted to protect the openings when not in use. Rats were allowed to recover from surgery for at least three days before acclimation began.

After recovery from surgery, animals were acclimated to chemical immobilization as described above. Following acclimation, fMRI was performed using the parameters described above for imaging using a 7 T MRI scanner (Bruker). 32 G internal cannula (Plastics One) preloaded with 1 μg/μL fluorescent muscimol (Thermo Fisher, Waltham, MA), were inserted prior to imaging, targeting VPM via the previously implanted guide cannulae. Each internal cannula was connected via tubing to a 10 μL Hamilton syringe. Internal cannulae extended 5–6 mm below the brain surface. Animals were then inserted into the MRI scanner. A 55 min EPI scan was initiated, allowing for the acquisition of 20 min of pre-injection resting state data, followed by infusion of 1.5 μL fluorescent muscimol at 0.10–0.15 μL/min, followed by the acquisition of an additional 20 min of resting state data after drug infusion. T_2w anatomical images were acquired before and after the resting state scan series.

Successful injections were confirmed by tracking the movement of a bubble at the interface of the fluorescent muscimol solution and oil filling the rest of the line from the injection pump. For a subset of animals, histological analysis was performed to directly assess the distribution of fluorescent muscimol after euthanasia. A spatially resolved assessment of injection volume was performed by measuring regions of T_2w contrast enhancement associated with fluid infusion. Fluid infusion transiently increases tissue water content, lowering the local transverse relaxation rate and brightening the signal in T_2w images. T_2w images acquired before and after infusion were therefore compared and the percent signal change was computed for each voxel in the ventral thalamus ROI that includes VPM (ThV in Supplementary Fig. 2), and also to an ROI corresponding to the posteromedial thalamus (Supplementary Fig. 9). For the eight animals from which both T_2w and rsFC data were available, values were compared with the changes in rsFC associated with treatment.

Facial stimulation

Seven chemically immobilized animals were included in a dataset on the effects of facial stimulation in fMRI; two additional animals were excluded on the basis of artifacts in the fMRI scans. Continuous or episodic facial stimulation was performed using air flow directed at the left and right vibrissa pads of each animal. Delivery of air pressurized by a Tetra Whisper Air Pump (Blacksburg, VA) was gated using solenoidal two-way valves toggled using a Raspberry Pi 4 (Cambridge, UK) controller synchronized with scanner operation, and flow was directed at the vibrissae by means of plastic tubing. For each animal, the placement of the air lines was chosen to displace several whiskers by at least 1 mm on each side, as assessed by visual inspection during continuous air flow.

To measure transient responses to blocks of unilateral facial stimulation, 10 Hz air pulses (50 ms/pulse) were delivered in 30 s blocks alternating with 60 s blocks in the absence of stimulation. This sequence was repeated six times for each side, during 10 min EPI acquisition scans performed using the same parameters applied for resting state analysis. Cortical voxels that showed significant responses to contralateral block stimuli across animals ($p < 0.05$) were identified and defined as response regions for each animal; animals that showed bilateral response regions were used for resting state analysis.

To measure the effects of continuous facial stimulation on rsFC in areas activated by block stimulation, two consecutive 25-minute EPI scan series were collected from each animal during the 10 Hz operation of the stimulator. The first EPI series was acquired with the system pressurized and the second was performed with the air pressure turned off. Animals were assumed to reach a steady state within five minutes, and only the last 20 min of each scan series were analyzed to determine the effects of airflow on rsFC. For these experiments, rsFC was evaluated using cortical ROIs for which the mean response to contralateral stimulation was significant across all animals ($p < 0.05$) that individually displayed both left and right responses to contralateral block stimulation ($n = 7$).

Vascular reactivity assessment

To compare vascular reactivity amplitudes between WT Sprague-Dawley and FXS model rats, we used fMRI to measure responses to hypercapnic challenges in two FXS and four WT animals. One further WT animal was scanned but excluded because it had a ventricular malformation. For these experiments, animals underwent no acclimation and were imaged under 1.5% isoflurane anesthesia with pancuronium paralysis and 7 T MRI parameters otherwise as described above. A 95 min EPI scan series was collected in each session. For the first 21 min of the scan, the animals were ventilated with an air and oxygen mixture at a ratio of 1:2. At 21 min, the oxygen was replaced with a 9:1 O_2:CO_2 mixture, leading to a final ratio of 5:9:1 air:O_2:CO_2 that contained 6.7% CO_2. At 51 min from the scan start time, the original gas mixture of 1:2 air:O_2 was restored and maintained for the remainder of the experiment.

Resting-state fMRI analysis

Images were reconstructed with Paravision 5.1 software (Bruker) and analyzed further using AFNI[68] and MATLAB (Mathworks, Natick, MA). Preprocessing steps for EPI data included removal of signal outside the brain, alignment to the anatomical scans using AFNI's *3dAllineate* function, motion correction using AFNI's *3dvolreg* function, spatial smoothing to 0.5 mm full width at half maximum using AFNI's *3dBlurToFWHM* function, and voxel-wise signal detrending and intensity normalization to convert voxel time courses to units of percent change from average baseline. Motion and global signals were regressed out of each dataset using MATLAB. Maximum motion coordinates were used to generate motion amplitude graphs.

Functional connectivity metrics were defined using seed-based regression analyses which enable better quantification of specific interregional effects and perturbation-linked amplitude changes, compared with correlational or independent components analyses. To generate seed-based functional connectivity maps, seed ROIs were defined using a standard brain atlas[69] or using air flow-responsive regions (Fig. 5 only) defined by voxels with significant activation across animals (t-test $p \le 0.05$, $n = 7$). Seedtime courses were computed by averaging the MRI signal over each ROI for each time point.

Regression analysis was then performed on a voxel-wise basis to determine the regression coefficient for each voxel relative to the seed. Functional connectivity matrices relating to pairs of ROIs were generated by computing seed time courses separately for each region in each animal and then performing within-animal regression analysis to determine the mean regression coefficient over voxels in each target ROI for each ROI-based seed region. The significance of regression coefficients or differences between coefficients was evaluated using two-sided Student's t tests over animals. Reported p-values presented throughout the text arise from uncorrected statistical tests performed across individual animals unless otherwise noted. Where indicated, false discovery rate (FDR) correction was applied using the *mafdr* function in MATLAB. Unless otherwise stated, all functional maps depict regression coefficients for voxels with uncorrected t test $p \le 0.01$ over animals. This comparatively liberal statistical threshold facilitates the comparison of regression amplitudes among multiple conditions while avoiding masking artifacts that more severe or data distribution-dependent statistical thresholds would have imposed.

Dynamic analysis of functional connectivity changes upon vibrissa inactivation was performed by assessing rsFC regression coefficients in sliding windows of five minutes over the 20-minute resting state time courses from each animal. Seed definitions and computations were otherwise as described above. To compare pre- and post-treatment results, mean rsFC coefficients before (M_{Pre}) and after (M_{Post}) vibrissa inactivation were calculated for each condition. Then the fraction of time for which the pre-treatment rsFC was above M_{Post} and the fraction of time for which post-treatment rsFC was above M_{Pre} was computed for each animal and presented in Supplementary Fig. 7.

To evaluate connectivity between S1BF and default mode network regions, we computed the mean regression coefficient describing interregional functional connectivity between S1BF (the seed region) and cingulate, parietal, and retrosplenial ROIs, weighted by the number of voxels in each DMN region. To quantify the local connectivity within S1BF, a single voxel seed was placed in the center of the S1BF ROI and the time course of this seed was used for a regression analysis against the rest of S1BF, yielding maps and mean values over S1BF. Welch's power spectral density functions were computed from resting state fMRI using the *pwelch* function in MATLAB. Results are plotted as $10 \log_{10} W$, where W is the output of *pwelch*.

Analysis of facial stimulation and vascular reactivity data

Data acquired during stimulation with airflow or carbogen challenge were analyzed largely as described for resting state analysis, but with minor differences. For block-design facial stimulation experiments, data were normalized to units of percent change with respect to the mean signal, and stimulus responses were computed as the percent signal observed 12–48 s after each stimulus onset minus the average signal observed 36–22 s before stimulus onset. ROI averages were evaluated over functionally defined ROIs, where cortical regions showing a significant response over animals ($n = 7$; $p \leq 0.05$) were used to assess rsFC amplitudes using methods otherwise as described above. For vascular reactivity tests, data were normalized and detrended with respect to the 21-minute baseline before administration of the CO_2-containing gas mixture, and signal changes observed during the 6.7% CO_2 inhalation period (35–45 min) were assessed with respect to this baseline.

Effective connectivity modeling

To assess whether vibrissa or thalamic inactivation resulted in changes to either effective connectivity or cortical and subcortical input we used Bayesian model comparison (BMC)[38], as implemented in the SPM12 statistical parametric mapping (SPM) software package (https://www.fil.ion.ucl.ac.uk/spm/software/spm12/). Following the extraction of the time series as described above, a spectral dynamic causal model (DCM) was specified for each subject. BMC then estimated the probability that a DCM model had generated the data of a specific subject in the group[39]. We compared four models where either the connectivity or the input, both, or neither were allowed to change following vibrissa or thalamus treatment ($n = 8, 9$). Input was parameterized as a function of frequency (f) as:

$$I_k(f) = I_{global} + S_k/f + \varepsilon \tag{1}$$

where k indexes brain regions (left and right S1BF and left and right sensory thalamus), $I_{global} = G_1/f^{G_2}$ is a global input with power law distribution shared across areas with coefficients G_1 and G_2, and $\varepsilon = H_1/f^{H_2}$ is a common observational noise term with coefficients H_1 and H_2[40,70]. On top of the global input, each brain area receives a specific $1/f$ input with amplitude S_k. In models where we assumed fixed input, the parameters S_k were fixed such that the sum of global and specific input to each region $I_{global} + S_k/f$ has a standard deviation of 1/8. This value was chosen to produce a maximum fMRI signal change of about 1%[71]. Other input parameters were allowed to change during fitting with the prior variance of 1/64, corresponding to a relatively lax confidence interval of 25%. In the rest of the models, S_k values were also given a prior variance of 1/64.

Model fits were evaluated after convergence. BMC then aggregated single subject probabilities to compute the exceedance probability (EP), defined as the probability of one model m_i being more likely than the alternative models $m_{j \neq i}$, across the subject group. EP can thus be expressed as

$$q_{m_i} = P\left(r_{m_i} > r_{m_{j \neq i}} \mid t\right) \tag{2}$$

where P denotes probability, t denotes the group fMRI data and r_{m_j} is the probability that model j generated the group data. To ensure that model fits were accurate we computed the proportion of explained variance for each subject using the SPM function *spm_dcm_fmri_check.m*.

To assess potential differences in effective connectivity arising from inactivation treatments in the different experimental groups, we used parametric empirical Bayes (PEB) analysis[40,41,72]. This allowed for a computationally efficient estimation of connectivity and neural parameters at the single subject level using the SPM routine *spm_dcm_fmri_csd.m*. Results were concatenated across subjects within each group and separately for each condition (*i.e.* before and after inactivation). Two analyses were then performed at the second level using the PEB method implemented in *spm_dcm_peb.m*. These yielded pre- and post-inactivation brain connectivity differences for each experiment. The PEB approach distinguishes between first-level models that generate subject-specific data and second-level linear models that contain explanatory variables at the group level, between subjects. These linear models map from group means to subject-specific connectivity estimates. Thus, first-level models are equipped with empirical priors that optimally shrink their parameter estimates to group means.

We focused on estimating group differences in effective connectivity due to vibrissa and thalamic inactivation treatments in the two conditions. We asked which, if any connectivity strengths (feedforward, feedback, and lateral) were different before *vs.* after the treatment in each condition. To do this, we tested all possible alternative models where each connection could vary or not. We compared models using the Bayesian model comparison that is implemented in the SPM PEB toolbox. This provides computationally expedient model fits and model parameters for each candidate model, defined in terms of a prior density.

These model parameters were used as regressors in a design matrix. Specifically, we compared the 34 nested candidate models diagrammed in Supplementary Fig. 10 using *spm_dcm_peb_bmc.m*. To avoid model dilution (individual model evidence becoming weak because of many similar models), we followed standard DCM practice and reduced the number of alternative models[73]. To account for bilateral perturbation, we considered 16 candidate models (models 1–15 and 32) that allow for symmetric changes in the left and right hemispheres. To accommodate changes due to unilateral perturbation, we also included 18 further models (models 16–31 and 33, 34) that are asymmetric variants of models 1–15 and 32. These allow for changes in the connections to and from the two thalamic or cortical areas to be different.

Each model was assessed using a free energy cost function[74], which expresses the model likelihood given the data. Following Bayesian model comparison, we also obtained estimates of random effects parameters using Bayesian model averaging. The likelihood that each model accounts for the experimental data is reported in Supplementary Fig. 10, while the specific connection strength changes that occurred with probability $p \geq 0.99$ (a subset of variable connection strengths in each case) are reported in Fig. 5.

Electrocorticography

Three adult rats were anaesthetized with isoflurane (3% for induction, 2% for maintenance) and head-fixed on a rodent stereotaxic instrument (Kopf), with a heating pad to maintain body temperature at 37 °C. The scalp was retracted, and a small craniotomy was drilled into the skull above the implantation site. Electrocorticography (ECoG) recording electrodes were constructed by soldering a Teflon-coated silver wire to a gold pin connector, and then briefly heated to create a spherical tip. The electrode was inserted through the craniotomy, directly under the skull, to be placed on top of the cortical surface above the somatosensory cortex (− 0.5 mm anterioposterior and + 3.5 mm mediolateral from bregma). A grounding screw was implanted into the cerebellum. The rats were then treated with 1 mg/kg slow-release buprenorphine subcutaneously to minimize pain and discomfort, prior to skin closure with suture and recovery from anesthesia on the heating pad. Animals were allowed 3–7 days for recovery before acclimation, as previously detailed for fMRI scan experiments.

ECoG recordings were performed after a minimum of two acclimation days on paralyzed, intubated, and ventilated animals, starting with the 2% isoflurane condition. The recording electrode was connected to a head stage, and signals were amplified using an extracellular amplifier (EXT-02F/2, npi Electronics, Tamm, Germany), low-pass filtered at 1 kHz, and digitized at 2 kHz. ECoG signals during different conditions were linearly detrended and plotted as a function of time to display signal characteristics. Power spectra of the raw ECoG traces were calculated using the same MATLAB routines used for fMRI analyses.

Statistics and reproducibility

Study designs, and statistical methods employed throughout the paper are described in context. No statistical method was used to predetermine the sample size. Data exclusion is noted above for each experiment, with most instances due to image artifacts or poor SNR. Randomization was not relevant to this study, as for nearly all experiments, each animal served as its own control (*i.e.* data are paired). The investigators were not blinded to allocation during experiments and outcome assessment.

Reporting summary

Further information on research design is available in the Nature Portfolio Reporting Summary linked to this article.

Data availability

Processed data are presented in the text, figures, and Supplementary Information. Source data are provided in this paper.

Code availability

No substantial code was produced as part of this study.

References

1. Power, J. D., Schlaggar, B. L. & Petersen, S. E. Studying brain organization via spontaneous fMRI signal. *Neuron* **84**, 681–696 (2014).
2. Gonzalez-Castillo, J., Kam, J. W. Y., Hoy, C. W. & Bandettini, P. A. How to interpret resting-state fMRI: Ask your participants. *J. Neurosci.* **41**, 1130–1141 (2021).
3. Biswal, B. B. Resting state fMRI: a personal history. *Neuroimage* **62**, 938–944 (2012).
4. Biswal, B., Yetkin, F. Z., Haughton, V. M. & Hyde, J. S. Functional connectivity in the motor cortex of resting human brain using echo-planar MRI. *Magn. Reson. Med.* **34**, 537–541 (1995).
5. Murphy, K., Birn, R. M. & Bandettini, P. A. Resting-state fMRI confounds and cleanup. *Neuroimage* **80**, 349–359 (2013).
6. Drew, P. J., Winder, A. T. & Zhang, Q. Twitches, blinks, and fidgets: Important generators of ongoing neural activity. *Neuroscientist* **25**, 298–313 (2019).
7. Shmuel, A. & Leopold, D. A. Neuronal correlates of spontaneous fluctuations in fMRI signals in monkey visual cortex: Implications for functional connectivity at rest. *Hum. Brain Mapp.* **29**, 751–761 (2008).
8. Keilholz, S. D. The neural basis of time-varying resting-state functional connectivity. *Brain Connect* **4**, 769–779 (2014).
9. Lu, H. et al. Low- but not high-frequency LFP correlates with spontaneous BOLD fluctuations in rat Whisker barrel cortex. *Cereb. Cortex* **26**, 683–694 (2016).
10. Baek, K. et al. Layer-specific interhemispheric functional connectivity in the somatosensory cortex of rats: resting state electrophysiology and fMRI studies. *Brain Struct. Funct.* **221**, 2801–2815 (2016).
11. Shi, Z. et al. On the relationship between MRI and local field potential measurements of spatial and temporal variations in functional connectivity. *Sci. Rep.* **9**, 8871 (2019).
12. Khalili-Mahani, N. et al. Biomarkers, designs, and interpretations of resting-state fMRI in translational pharmacological research: A review of state-of-the-Art, challenges, and opportunities for studying brain chemistry. *Hum. Brain Mapp.* **38**, 2276–2325 (2017).
13. Orefice, L. L. Outside-in: Rethinking the etiology of autism spectrum disorders. *Science* **366**, 45–46 (2019).
14. Winder, A. T., Echagarruga, C., Zhang, Q. & Drew, P. J. Weak correlations between hemodynamic signals and ongoing neural activity during the resting state. *Nat. Neurosci.* **20**, 1761–1769 (2017).
15. Schroeter, A., Grandjean, J., Schlegel, F., Saab, B. J. & Rudin, M. Contributions of structural connectivity and cerebrovascular parameters to functional magnetic resonance imaging signals in mice at rest and during sensory paw stimulation. *J. Cereb. Blood Flow Metab.* **37**, 2368–2382 (2017).
16. Wang, X., Leong, A. T. L., Chan, R. W., Liu, Y. & Wu, E. X. Thalamic low frequency activity facilitates resting-state cortical interhemispheric MRI functional connectivity. *Neuroimage* **201**, 115985 (2019).
17. Jung, W. B., Jiang, H., Lee, S. & Kim, S. G. Dissection of brain-wide resting-state and functional somatosensory circuits by fMRI with optogenetic silencing. *Proc. Natl. Acad. Sci. USA* **119**, e2113313119 (2022).
18. Ferris, C. F. Applications in awake animal magnetic resonance imaging. *Front. Neurosci.* **16**, 854377 (2022).
19. Ferrier, J., Tiran, E., Deffieux, T., Tanter, M. & Lenkei, Z. Functional imaging evidence for task-induced deactivation and disconnection of a major default mode network hub in the mouse brain. *Proc. Natl. Acad. Sci. USA* **117**, 15270–15280 (2020).
20. Gutierrez-Barragan, D. et al. Unique spatiotemporal fMRI dynamics in the awake mouse brain. *Curr. Biol.* **32**, 631–644 (2022).
21. Musall, S., Kaufman, M. T., Juavinett, A. L., Gluf, S. & Churchland, A. K. Single-trial neural dynamics are dominated by richly varied movements. *Nat. Neurosci.* **22**, 1677–1686 (2019).
22. Peeters, R. R., Tindemans, I., De Schutter, E. & Van der Linden, A. Comparing BOLD fMRI signal changes in the awake and anesthetized rat during electrical forepaw stimulation. *Magn. Reson. Imaging* **19**, 821–826 (2001).
23. Kumstel, S. et al. Grading distress of different animal models for gastrointestinal diseases based on plasma corticosterone kinetics. *Animals* **9**, 145 (2019).
24. Gong, S. et al. Dynamics and correlation of serum cortisol and corticosterone under different physiological or stressful conditions in mice. *PLoS ONE* **10**, e0117503 (2015).
25. Benedetti, M. et al. Plasma corticosterone levels in mouse models of pain. *Eur. J. Pain.* **16**, 803–815 (2012).
26. Chang, C. & Glover, G. H. Time-frequency dynamics of resting-state brain connectivity measured with fMRI. *Neuroimage* **50**, 81–98 (2010).
27. Keilholz, S. D., Magnuson, M. E., Pan, W. J., Willis, M. & Thompson, G. J. Dynamic properties of functional connectivity in the rodent. *Brain Connect* **3**, 31–40 (2013).
28. Buckner, R. L. The serendipitous discovery of the brain's default network. *Neuroimage* **62**, 1137–1145 (2012).
29. Raichle, M. E. The brain's default mode network. *Annu. Rev. Neurosci.* **38**, 433–447 (2015).
30. Baek, K., Park, C. R., Jang, S., Shim, W. H. & Kim, Y. R. Anesthetic modulations dissociate neuroelectric characteristics between sensory-evoked and spontaneous activities across bilateral rat somatosensory cortical laminae. *Sci. Rep.* **12**, 11661 (2022).
31. Diamond, M. E., Armstrong-James, M., Budway, M. J. & Ebner, F. F. Somatic sensory responses in the rostral sector of the posterior group (POm) and in the ventral posterior medial nucleus (VPM) of the rat thalamus: dependence on the barrel field cortex. *J. Comp. Neurol.* **319**, 66–84 (1992).
32. Diamond, M. E., Armstrong-James, M. & Ebner, F. F. Somatic sensory responses in the rostral sector of the posterior group (POm) and in the ventral posterior medial nucleus (VPM) of the rat thalamus. *J. Comp. Neurol.* **318**, 462–476 (1992).
33. Wang, H., Standifer, K. M. & Sherry, D. M. GABA(A) receptor binding and localization in the tiger salamander retina. *Vis. Neurosci.* **17**, 11–21 (2000).
34. El-Boustani, S. et al. Anatomically and functionally distinct thalamocortical inputs to primary and secondary mouse whisker somatosensory cortices. *Nat. Commun.* **11**, 3342 (2020).

35. Friston, K. J. Functional and effective connectivity: a review. *Brain Connect* **1**, 13–36 (2011).
36. Friston, K. J., Harrison, L. & Penny, W. Dynamic causal modelling. *Neuroimage* **19**, 1273–1302 (2003).
37. Bernal-Casas, D., Lee, H. J., Weitz, A. J. & Lee, J. H. Studying brain circuit function with dynamic causal modeling for optogenetic fMRI. *Neuron* **93**, 522–532 (2017).
38. Penny, W. D. et al. Comparing families of dynamic causal models. *PLoS Comput. Biol.* **6**, e1000709 (2010).
39. Stephan, K. E., Penny, W. D., Daunizeau, J., Moran, R. J. & Friston, K. J. Bayesian model selection for group studies. *Neuroimage* **46**, 1004–1017 (2009).
40. Friston, K. J., Kahan, J., Biswal, B. & Razi, A. A DCM for resting state fMRI. *Neuroimage* **94**, 396–407 (2014).
41. Pinotsis, D. A., Perry, G., Litvak, V., Singh, K. D. & Friston, K. J. Intersubject variability and induced gamma in the visual cortex: DCM with empirical Bayes and neural fields. *Hum. Brain Mapp.* **37**, 4597–4614 (2016).
42. Redcay, E. et al. Intrinsic functional network organization in high-functioning adolescents with autism spectrum disorder. *Front. Hum. Neurosci.* **7**, 573 (2013).
43. Orefice, L. L. et al. Targeting peripheral somatosensory neurons to improve tactile-related phenotypes in ASD models. *Cell* **178**, 867–886 (2019).
44. Hamilton, S. M. et al. Fmr1 and Nlgn3 knockout rats: novel tools for investigating autism spectrum disorders. *Behav. Neurosci.* **128**, 103–109 (2014).
45. Zhang, Y. et al. Dendritic channelopathies contribute to neocortical and sensory hyperexcitability in Fmr1(-/y) mice. *Nat. Neurosci.* **17**, 1701–1709 (2014).
46. Haberl, M. G. et al. Structural-functional connectivity deficits of neocortical circuits in the Fmr1 (-/y) mouse model of autism. *Sci. Adv.* **1**, e1500775 (2015).
47. Betti, V. et al. Natural scenes viewing alters the dynamics of functional connectivity in the human brain. *Neuron* **79**, 782–797 (2013).
48. Vanderwal, T., Kelly, C., Eilbott, J., Mayes, L. C. & Castellanos, F. X. Inscapes: A movie paradigm to improve compliance in functional magnetic resonance imaging. *Neuroimage* **122**, 222–232 (2015).
49. Costumero, V., Bueicheku, E., Adrian-Ventura, J. & Avila, C. Opening or closing eyes at rest modulates the functional connectivity of V1 with default and salience networks. *Sci. Rep.* **10**, 9137 (2020).
50. Cauda, F. et al. Low-frequency BOLD fluctuations demonstrate altered thalamocortical connectivity in diabetic neuropathic pain. *BMC Neurosci.* **10**, 138 (2009).
51. Rocca, M. A. et al. Brain connectivity abnormalities extend beyond the sensorimotor network in peripheral neuropathy. *Hum. Brain Mapp.* **35**, 513–526 (2014).
52. Wang, D. et al. Altered resting-state network connectivity in congenital blind. *Hum. Brain Mapp.* **35**, 2573–2581 (2014).
53. Dell Ducas, K. et al. Functional and structural brain connectivity in congenital deafness. *Brain Struct. Funct.* **226**, 1323–1333 (2021).
54. Felger, J. C. et al. Inflammation is associated with decreased functional connectivity within corticostriatal reward circuitry in depression. *Mol. Psychiatry* **21**, 1358–1365 (2016).
55. Marsland, A. L. et al. Systemic inflammation and resting state connectivity of the default mode network. *Brain Behav. Immun.* **62**, 162–170 (2017).
56. Schrepf, A. et al. A multi-modal MRI study of the central response to inflammation in rheumatoid arthritis. *Nat. Commun.* **9**, 2243 (2018).
57. Swartz, J. R. et al. Associations between peripheral inflammation and resting state functional connectivity in adolescents. *Brain Behav. Immun.* **95**, 96–105 (2021).
58. Bagga, D. et al. Influence of 4-week multi-strain probiotic administration on resting-state functional connectivity in healthy volunteers. *Eur. J. Nutr.* **58**, 1821–1827 (2019).
59. Curtis, K. et al. Insular resting state functional connectivity is associated with gut microbiota diversity. *Eur. J. Neurosci.* **50**, 2446–2452 (2019).
60. Greicius, M. Resting-state functional connectivity in neuropsychiatric disorders. *Curr. Opin. Neurol.* **21**, 424–430 (2008).
61. Jack, A. Neuroimaging in neurodevelopmental disorders: focus on resting-state fMRI analysis of intrinsic functional brain connectivity. *Curr. Opin. Neurol.* **31**, 140–148 (2018).
62. Yu, T. W. & Berry-Kravis, E. Autism and fragile X syndrome. *Semin Neurol.* **34**, 258–265 (2014).
63. Hall, S. S., Jiang, H., Reiss, A. L. & Greicius, M. D. Identifying large-scale brain networks in fragile X syndrome. *JAMA Psychiatry* **70**, 1215–1223 (2013).
64. Arnett, M. T., Herman, D. H. & McGee, A. W. Deficits in tactile learning in a mouse model of fragile X syndrome. *PLoS ONE* **9**, e109116 (2014).
65. Berzhanskaya, J., Phillips, M. A., Shen, J. & Colonnese, M. T. Sensory hypo-excitability in a rat model of fetal development in Fragile X Syndrome. *Sci. Rep.* **6**, 30769 (2016).
66. Smith, S. D., Nadeau, C., Sorokopud-Jones, M. & Kornelsen, J. The relationship between functional connectivity and interoceptive sensibility. *Brain Connect* **12**, 417–431 (2021).
67. Hohaia, W., Saurels, B. W., Johnston, A., Yarrow, K. & Arnold, D. H. Occipital alpha-band brain waves when the eyes are closed are shaped by ongoing visual processes. *Sci. Rep.* **12**, 1194 (2022).
68. Cox, R. W. AFNI: software for analysis and visualization of functional magnetic resonance neuroimages. *Comput. Biomed. Res.* **29**, 162–173 (1996).
69. Paxinos, G. & Watson, C. *The Rat Brain In Stereotaxic Coordinates*, Compact 6th Ed. (Academic Press, New York; 2009).
70. Bullmore, E. et al. Colored noise and computational inference in neurophysiological (fMRI) time series analysis: resampling methods in time and wavelet domains. *Hum. Brain Mapp.* **12**, 61–78 (2001).
71. Welvaert, M. & Rosseel, Y. On the definition of signal-to-noise ratio and contrast-to-noise ratio for FMRI data. *PLoS ONE* **8**, e77089 (2013).
72. Razi, A., Kahan, J., Rees, G. & Friston, K. J. Construct validation of a DCM for resting state fMRI. *Neuroimage* **106**, 1–14 (2015).
73. Zeidman, P. et al. A guide to group effective connectivity analysis, part 2: Second level analysis with PEB. *Neuroimage* **200**, 12–25 (2019).
74. Friston, K., Kilner, J. & Harrison, L. A free energy principle for the brain. *J. Physiol. Paris* **100**, 70–87 (2006).

Acknowledgements

This research was funded by grants from the MIT Simons Center for the Social Brain, the K. Lisa Yang Brain-Body Center, and the NIH (R01 NS121073, R01 DA038642) to A.J. and S.B. was supported by a J. Douglas Tan Postdoctoral Fellowship from the McGovern Institute for Brain Research; S.B. and M. Dawson were also funded by the MIT Neurobiological Engineering Training Program (NIH grant T32 EB019940). M.S. was the recipient of a Marie Curie Individual Fellowship from the European Commission. N.L. was supported by a Stanley Fahn Research Fellowship from the Parkinson's Disease Foundation, and KSC was a Lore Harp McGovern Graduate Student Fellow. D.A.P. was supported by grant UKRI ES/T01279X/1. The authors thank Susan Whitfield-Gabrieli for technical guidance and comments on the manuscript.

Author contributions

S.B. and A.J. designed the study. S.B. and M. Desai established the chemically immobilized rat fMRI preparation. S.B. led the data collection with assistance from M. Dawson, J.L., M. Desai, M.S., E.D., E.F., N.L., and A.B. K.S.C. designed the airflow stimulator. S.M. performed mystacial pad histology. J.P.F. and D.A.P. performed the effective connectivity analysis. S.B. performed the data analysis, and S.B. and A.J. wrote the paper with help from the other authors.

Competing interests

The authors declare no competing interests.

Additional information

Supplementary information The online version contains supplementary material available at https://doi.org/10.1038/s41467-024-55064-6.

Correspondence and requests for materials should be addressed to Alan Jasanoff.

Peer review information *Nature Communications* thanks Young Kim, and the other anonymous reviewer(s) for their contribution to the peer review of this work.

Reprints and permissions information is available at http://www.nature.com/reprints

Publisher's note Springer Nature remains neutral with regard to jurisdictional claims in published maps and institutional affiliations.

Open Access This article is licensed under a Creative Commons Attribution-NonCommercial-NoDerivatives 4.0 International License, which permits any non-commercial use, sharing, distribution and reproduction in any medium or format, as long as you give appropriate credit to the original author(s) and the source, provide a link to the Creative Commons licence, and indicate if you modified the licensed material. You do not have permission under this licence to share adapted material derived from this article or parts of it. The images or other third party material in this article are included in the article's Creative Commons licence, unless indicated otherwise in a credit line to the material. If material is not included in the article's Creative Commons licence and your intended use is not permitted by statutory regulation or exceeds the permitted use, you will need to obtain permission directly from the copyright holder. To view a copy of this licence, visit http://creativecommons.org/licenses/by-nc-nd/4.0/.

© The Author(s) 2024